Numerical Study on the Effect of Electrode Geometry in MPD Thrusters

IEPC-2011-228

Presented at the 32nd International Electric Propulsion Conference,
Wiesbaden • Germany
September 11 – 15, 2011

M. Mahendhran[1] and Amit Kumar[2]
Indian Institute of Technology Madras, Chennai-600 036, India

The self-field MPD thruster is numerically modeled in 2D and axisymmetric configurations. The model comprises of inviscid, compressible, magnetohydrodynamic flow of fully ionized argon plasma. A validated finite volume numerical code has been used to simulate a 2D MPDT (the geometry of which is based on the previous experiments) and an equivalent coaxial thruster (based on equal electromagnetic thrust) for a comparative study. The dependence of thruster performance on cathode length for the two thrusters has been studied at various inlet mass flow rates and currents. The simulations show that shorter cathodes results in higher thrust and specific impulse compared to longer cathodes. This observation is consistent with previously reported experiments. It is also noted that the rate of drop in thrust and specific impulse with cathode length decreases with increase in cathode length. The effect of cathode length also diminishes as the thruster operation is shifted to electromagnetic regime (where electromagnetic thrust component dominates total thrust). These observation imply that the effect of cathode length on thruster performance to be a thermal phenomenon. The equivalent coaxial thruster shows similar performance characteristics as the 2D thruster except for higher sensitivity to short cathode length on thruster performance compared to the 2D counterpart.

Nomenclature

2D	=	two-dimensional
Δx	=	grid size in x-direction
α	=	co-efficient to specify the amount of current through cathode tip
β	=	electron Hall parameter
ε_0	=	permittivity of free space(=8.854× 10^{-12} farad/m)
μ_0	=	magnetic permeability of free space(=4π× 10^{-7} henry/m)
κ	=	Boltzmann constant (=1.38 × 10^{-23} J/K)
ρ	=	density
σ	=	electrical conductivity
Ω	=	volume of the cell(area in 2D)
ω_e	=	gyro frequency of electrons
τ_e	=	collision time of electrons
ψ	=	magnetic stream function
$\mathbf{B}$	=	self induced magnetic field
B_0	=	self induced magnetic field at inlet
d	=	diameter

[1] M.S. Scholar, Department of Aerospace Engineering, mmahendhran@gmail.com
[2] Associate Professor, Department of Aerospace Engineering, amitk@ae.iitm.ac.in

dl = elemental contour length
ds = elemental surface area
e = charge of a proton(=1.602× 10^{-19} C)
e_t = total specific energy of the fluid
E = electric field
F = thrust
$\mathbf{F_C}$ = convective fluxes
g_0 = gravitational acceleration on earth (=9.81 m/s^2)
I = input current
I_{sp} = specific impulse
j = current density
$\dot{m}$ = inlet mass flow rate
M = Mach number
MPDT = Magnetoplasmadynamic Thruster
n = outward normal vector
n_e = number density of electrons
p = pressure
R_{gas} = specific gas constant
r,θ,x = cylindrical coordinates
t = time
t = unit tangent vector
T = temperature
TPR = thrust to power ratio
U = conserved variables
v = velocity vector (u, v components)
W = width of the channel in 2D MPDT
x,y,z = Cartesian coordinates

Subscripts
a = anode
c = cathode
coax = coaxial
em = electromagnetic

I. Introduction

THE combination of high I_{sp}, high thrust density and simple design make Magnetoplasmadynamic thrusters(MPDT) an attractive option of electric propulsion for deep space missions, provided the feasibility of high power availability in space. Understanding of various physical processes and their interaction inside these thrusters would help to model them to a greater degree of accuracy, which could lead to the design of efficient thrusters.

The dependence of thruster performance on geometric configuration has been studied previously using analytical,[1,2] experimental[3,4] and numerical approaches.[5-7] These studies[1-6] reported efficient performance of convergent-divergent anode configurations over straight and flared anode configurations. The experimental[4] observations from 2D MPDTs showed better thruster performance (thrust and specific impulse) with short a cathode, which was attributed to the higher electro-thermal component in thrust. The numerical work on 2D MPDT[5] with flared and convergent divergent anode also found short cathode contained within the throat region performed better. This increase in performance was observed in the I_{sp} range of 1000-3000 s, above which this effect was not observed.[4] Other configurations such as the cathode embedded near the thruster inlet have also shown better performance of 2D thrusters.[6]

The objective of the present study is to understand and compare the effect of cathode length in 2D and equivalent coaxial thrusters. The dimensions of the 2D thrusters were taken from the 2D MPDT experiments[4] and the dimension of the coaxial thruster was obtained to produce equivalent electromagnetic thrust, the details of which will be described later. A numerical model in 2D and axisymmetric co-ordinates has been developed and used for this study. The details of this model are described next.

II. Formulation of the Model

A. Assumptions

1) Gaseous argon is used as the propellant. It is considered as completely singly ionized and quasi-neutral plasma as it enters the thrust chamber.
2) Plasma is considered inviscid and thermally non-conducting perfect gas. Complex processes like electrical sheath formation and radiation heat transfer are neglected.
3) Secondary effects such as ion slip in Ohm's law and displacement current in Ampere's law are not considered.
4) Electrical conductivity of the plasma is taken as a scalar function of temperature and density, given by Spitzer-Harm's formulation for fully ionized plasma.
5) Plasma flow is two-dimensional (x-y plane) and the magnetic field acts only in the z-direction for 2D-MPDT. In case of coaxial thruster, the flow is axisymmetric (x-r plane) and magnetic field acts only in the azimuthal (θ) direction.

B. Governing Equations

The integral form of generic conservation equations for inviscid, adiabatic flow with external body force and external power input are used for the computational modeling.

Mass conservation equation:

$$\frac{\partial}{\partial t}\int_{\Omega} \rho d\Omega + \oint_{s} \rho \mathbf{v}\cdot \mathbf{n} ds = 0 \tag{1}$$

Momentum Equation:

$$\frac{\partial}{\partial t}\int_{\Omega} \rho \mathbf{v} d\Omega + \oint_{s} \rho \mathbf{v}\mathbf{v}\cdot \mathbf{n} ds = -\oint_{s} p\mathbf{n} ds + \int_{\Omega} \mathbf{j}\times\mathbf{B} d\Omega \tag{2}$$

Energy Equation:

$$\frac{\partial}{\partial t}\int_{\Omega} \rho e_t d\Omega + \oint_{s} (\rho e_t + p)\mathbf{v}\cdot \mathbf{n} ds = \int_{\Omega} \mathbf{j}\cdot \mathbf{E} d\Omega \tag{3}$$

Equation of State:

$$p = \rho R_{gas} T \tag{4}$$

Combining Ampere's law and Faraday's law in Maxwell's equation with Ohm's law, a single equation in terms of magnetic flux density is derived.

Ampere's law:

$$\nabla\times\mathbf{B} = \mu_0 \mathbf{j} \tag{5}$$

Faraday's law:

$$\nabla\times\mathbf{E} = -\partial\mathbf{B}/\partial t \tag{6}$$

Ohm's law:

$$\mathbf{j} = \sigma[\mathbf{E} + \mathbf{v}\times\mathbf{B} - \beta(\mathbf{j}\times\mathbf{B})] \tag{7}$$

Equation of Magnetic flux density:

$$\frac{\partial\mathbf{B}}{\partial t} - \nabla\times(\mathbf{v}\times\mathbf{B}) + \nabla\times(\frac{1}{\sigma\mu_0}\nabla\times\mathbf{B}) + \nabla\times(\frac{\beta}{\mu_0}(\nabla\times\mathbf{B})\times\mathbf{B}) = 0 \tag{8}$$

Electrical conductivity for fully ionized plasma is given by Spitzer-Harm formulation[5,8,9]

$$\sigma = 1.5\times 10^{-2}\frac{T^{3/2}}{\ln\Lambda} \tag{9}$$

Where Coulomb logarithm $\ln\Lambda$ is $\ln\Lambda = \ln\left[\frac{12\sqrt{2}\pi\varepsilon_0^{3/2}(\kappa T)^{3/2}}{e^3 n_e^{1/2}}\right]$

The electron Hall parameter is taken as[8,10]

$$\beta = \frac{\omega_e \tau_e}{|B|\sigma} = \frac{1}{en_e} \tag{10}$$

All the variables in the above equations are non-dimensionalized with chosen reference quantities[1,9] and the governing equations in non-dimensional form are used for the numerical solution.

C. Numerical Approach

1. Spatial Discretization of Flow Equations

A dual control volume, vertex centered finite volume method[11-14] is used to discretize the spatial terms in the governing equations. The convective fluxes are computed using a 6-point average scheme.[15] Jameson's artificial dissipation is added to stabilize the solution as a central type discretization is used for the convective fluxes.[11,13] It also helps in stabilizing the solution in the regions of shocks where the flow variables encounter high gradients. The spatially discretized system of equations result in a system of ordinary differential equations of the form:

$$\frac{d}{dt}(\mathbf{U}\Omega)_{i,j} + \sum_{faces}[(\mathbf{F}_{\mathbf{c},x} n_x + \mathbf{F}_{\mathbf{c},y/r} n_{y/r})ds]_{i,j} = (\mathbf{Q}\Omega)_{i,j} \tag{11}$$

The subscripts y and r are used to indicate that a similar discretization methodology is followed in 2D and coaxial cases, with suitable modifications in the surface area vectors in flux terms in case of cylindrical coordinates.

2. Spatial Discretization of Magnetic field Equation:

The integral form of Faraday's law [Eq. (12)] is discretized[16] similar to flow equations with an averaging scheme for convective terms. The gradient/derivative terms are evaluated using auxiliary control volumes formed around the cell faces and applying Green's theorem to compute the integral divided by the area of the auxiliary control volume

$$\iint_s \frac{\partial \mathbf{B}}{\partial t} \mathbf{n} ds = \oint_c \mathbf{E} \cdot \mathbf{t} dl \tag{12}$$

In the 2D model, the magnetic field (B_z) is discretized directly [Eq. (13)], whereas in the axisymmetric model, the azimuthal component of the magnetic field (B_θ) is computed in terms of magnetic stream function ($\psi = rB_\theta$) as in Eq. (14)

$$\Omega_{cell} \frac{\partial \mathbf{B}_{i,j}}{\partial t} = -\sum_{faces}(\mathbf{E} \cdot \mathbf{t} ds) \tag{13}$$

$$\frac{\partial \psi_{i,j}}{\partial t} = -\frac{r_{i,j}}{\Omega_{2D}} \sum_{faces}(\mathbf{E} \cdot \mathbf{t} ds) \tag{14}$$

The Electric field ($\mathbf{E}$) is obtained from Ohm's law and the current density ($\mathbf{j}$) is obtained from Ampere's law.

3. Time Integration:

The discretize form of ordinary differential equations of flow are marched in time using classical fourth order Runge-Kutta method. The time step used for the explicit marching is deduced from a CFL condition taken for a cell vertex finite volume method.[17] To enable the computation of unsteady flow fields, a global time stepping approach is followed.

Since the time scale of the magnetic diffusion involved in the MHD equation is of the order of $\Delta x^2/(1/\sigma\mu_0)$, which is 2-3 orders less than the typical flow time scales.[18] The simultaneous solution of flow and magnetic field equation imposes severe restriction on the size of the time step used, therefore the magnetic induction equation is solved separately at each flow time step enabling a faster computation. The magnetic induction equation is integrated in time by an implicit Euler method coupled with Alternating Direction Implicit (ADI) method using Thomas algorithm for the solution of the resulting Tri-Diagonal Matrix(TDM) form of equations. This procedure allows the usage of larger time steps and also ensures better numerical stability compared to the explicit methodology. The time step used for the magnetic field equation is of the order 10^{-9} -10^{-10} s in both 2D and coaxial thruster models.

4. Boundary Conditions

Flow

A subsonic inflow is maintained at inlet for 2D thruster, where from known values of inlet mass flow rate and temperature, density is extrapolated from interior domain to fix the velocity. Other variables are determined from the known values. A supersonic inflow is prescribed for coaxial thruster inlet, due to the tendency of the flow to have higher/supersonic velocities near the cathode tip resulting from larger Lorentz force causing numerical instability. The supersonic inflow is maintained by prescribing all the flow variables, deduced from known values of mass flow rate and temperature at inlet and also choosing a supersonic Mach number at the inlet. A supersonic outflow is maintained at the exit section, where all variables are extrapolated. Electrode and insulator surfaces are maintained as slip walls with adiabatic boundary condition for temperature. The axis is treated as a symmetry boundary, where there are no gradients in all flow variables and a zero velocity component across the axis is maintained.

Electromagnetic

The magnetic field at the inlet is prescribed according to Ampere's law, which results in a constant value of magnetic field for 2D thruster and a function of radius for coaxial thruster. Since a stream function formulation ($\psi = rB_\theta$) is used in case of axisymmetric model, a constant value of ψ is prescribed at inlet.

$$B_{z,inlet} = \mu_0 I/(2W) \tag{15}$$

$$\psi_{inlet} = \mu_0 I/(2\pi) \tag{16}$$

$B_{z,inlet}/\psi_{inlet}$ is maintained in the upstream insulators too, when they are present. The electrodes are maintained at a constant potential, which implies a zero tangential component of electric field on the electrode surface. B_z/ψ is fixed there discretizing the tangential electric field relation. At axis, outer insulators and exit, $B_z/\psi=0$ is maintained, so that the current does not cross these boundaries.

The convergence of the numerical solution is monitored using L2 norm error in computing the scaled & absolute residuals of continuity, x and y-momentum and energy equations. In addition, L∞ norm error in pressure and the error in the net mass flow rate crossing the domain boundaries are also monitored. The error of the magnetic field computation is monitored separately at each flow time step. The solution after the least possible and unaltered value of residual/error is taken as the final converged solution.

D. Thruster Performance Parameters

To assess the thruster performance, the output parameters of interest typical to electric propulsion thrusters are computed from the final solution.

I. Total thrust

$$F_{total} = F_{momentum} + F_{pressure} = \int_{exit\ section} \rho \mathbf{v}(\mathbf{v}\cdot \mathbf{n})ds + (p_{exit} - p_{ambient})A_{exit} \tag{17}$$

The exit of thruster is assumed to be at vacuum and hence $p_{ambient} = 0$ Pa is used.

II. Electromagnetic thrust is computed as

$$F_{em} = \int_{\Omega} (\mathbf{j} \times \mathbf{B})_x d\Omega = \int_{\Omega} j_{y/r} B_{z/\theta} d\Omega \tag{18}$$

III. Thermal thrust can be defined using the definitions of total and electromagnetic thrusts

$$F_{thermal} = F_{total} - F_{em} \tag{19}$$

IV. Specific impulse

$$I_{sp} = \frac{F_{total}}{\dot{m} g_0} \tag{20}$$

V. Input Power

$$Input\ \ Power = \int_{\Omega} \mathbf{j} \cdot \mathbf{E} d\Omega \tag{21}$$

VI. Thrust to Power Ratio (TPR) computed as a measure of thrust produced per kW of electrical energy expended

$$TPR = \frac{F_{total}}{Input\ \ Power} \tag{22}$$

E. Validation of Numerical Model

The numerical model of 2D and coaxial thrusters are validated separately against available experimental and numerical results.

1. *Two-Dimensional MPDT*

A 2D domain resembling the top portion of the experimental thruster schematically shown in Fig. 1 is used for the validation following Ref. 5, where in numerical and experimental results are presented. The computational domain has an extra insulator region attached to the anode instead of the abrupt end (as in schematic), which would prevent failure of computation due the sudden expansion region aft of the anode, since an inviscid flow model is employed. Hall current is not included and the domain is discretized with 51×31 grid points clustered near inlet region (inset in Fig. 1). The boundary condition at the inlet correspond to a subsonic flow (M_{inlet} = 0.3), with a mass flow rate of 2.5 g/s and T_{inlet} = 5000 K and a current of I= 8 kA.

The axial velocity along a horizontal line through the thruster taken at a height of 9 mm from the thruster axis (inset in Fig. 2) is compared with the numerical results of Ref. 5. A qualitative match of the results can be seen, even though the magnitude in the present computation is lesser than the values of Ref. 5 throughout. Neglecting the small values of pressure thrust, the momentum thrust computed at the end of anode section is plotted as a function of discharge current along with the experimental and numerical values.[5]

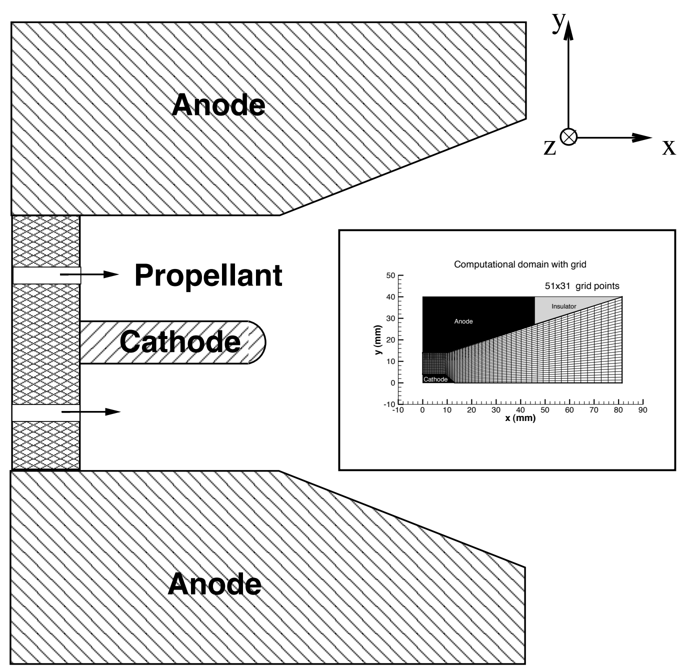

Figure 1. Schematic of the 2D MPDT with computational domain shown as an inset

The present result predicts higher values of thrust throughout, but the trend is qualitatively similar. The solution was tested for grid independence with the scaling factors of 0.5, 0.75, 1.5 and 2 on the 51×31 grid. A standard deviation of 4 % from the mean value of thrust was observed.

The mismatch in axial velocity and thrust plots between the present results and that of Ref. 5 may be due to the difference in the computational techniques used. A TVD-Mac Cormack scheme with Roe's dissipation is employed for discretization of convective fluxes in a generalized coordinate finite-difference framework in Ref. 5, whereas an averaging scheme with Jameson's artificial dissipation is used in a finite-volume framework in the present model.

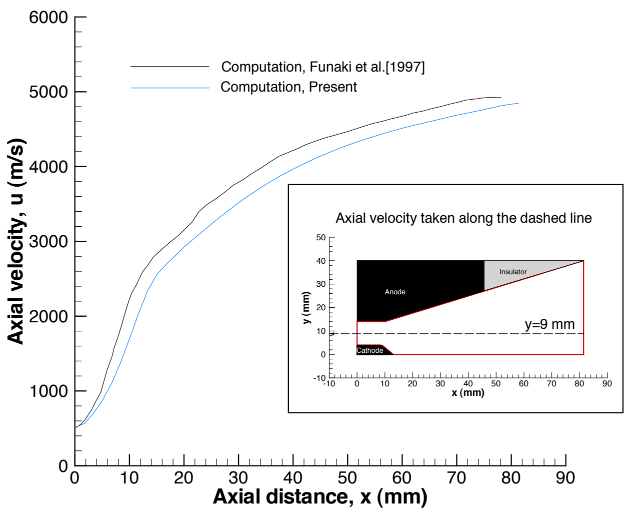

Figure 2. Axial velocity along the thruster with line of extraction in the domain shown as inset

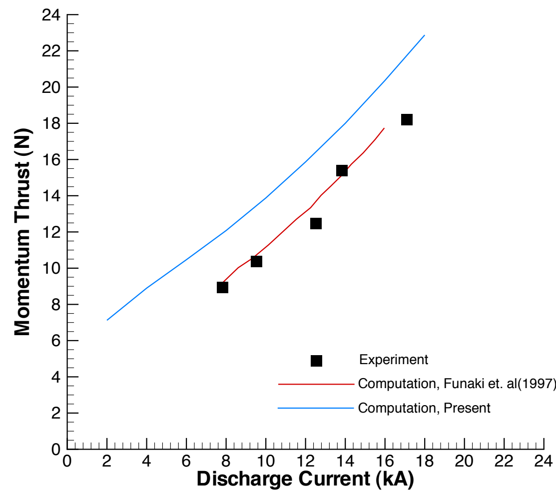

Figure 3. Thrust at different currents

2. *Coaxial MPDT*

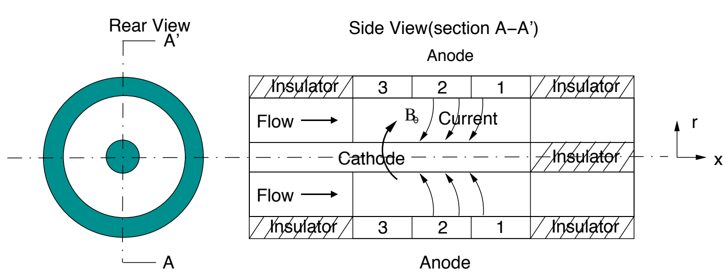

Figure 4. Schematic of the Coaxial MPDT

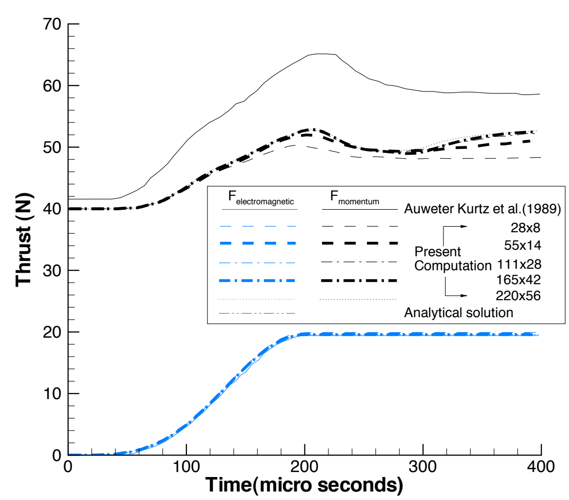

Figure 5. Thrust as a function of time

A simplified model of the ZT-1 thruster (Fig. 4) developed and tested at Institute of Space Systems(IRS), Stuttgart-Germany[10] is considered for the numerical simulation to validate the coaxial MPD thruster code. The thruster has 90 mm long coaxial electrodes. The radii of cathode and anode are 9 mm and 35 mm, respectively. The domain considered for computation is the top section, with a symmetric flow assumption about the central axis. The computation is carried out with the following flow conditions: M_{inlet} = 1.2, mass flow rate of 20 g/s, T_{inlet} = 8000 K and I = 12 kA. Ref. 10 used a uniform grid with 55×14 points. The same 55×14 uniformly spaced grid points are used initially, then various grid sizes corresponding to the factors 0.5, 2, 3, and 4 on the 55×14 are used. To avoid the inherent instability due to the shock formation inside the thruster at the instant of application of high current, the input current is given as a gradually increasing function, $I=I_{max}\sin^2[\pi t/(2t_{final})]$ with the maximum current (I_{max}=12 kA) attained over a period of t_f=200 μs, thereafter the current is maintained at 12 kA.

Figure. 5 shows the variation of the momentum thrust and the electromagnetic thrust computed at the exit as a function of time over a range of 0-400 μs. It can be observed that both thrust components increase with increasing current. The electromagnetic thrust matches closely with the results of Ref. 10 and the theoretical value, the expression for the theoretical electromagnetic thrust for coaxial cylindrical MPDT is[19]

$$F_{em,theoretical} = \frac{\mu_0 I^2}{4\pi}\ln\left(\frac{r_a}{r_c}\right) \tag{23}$$

The above expression gives a thrust of 19.56 N for 12 kA total input current. The variation in results is only 0.5 % for the 55×14 grid. There is an under prediction in the total thrust compared to Ref. 10, which is due to the variation in exit mass flow. Ref. 10 reports an increase of around 10 % in the exit mass flow rate, whereas the present computation shows a decrease of 3 % for the 55×14 grid.

III. Discussion of Results

As mentioned before, the variation in cathode length has been shown to have an effect on thruster performance in 2D MPD thrusters.[4,5] and it was seen that short cathodes performed better in terms of thrust/I_{sp}. Here in this study, we examine this effect numerically. First, a 2D geometry similar to the one used by Ref. 4 is examined followed by a comparative study on an equivalent coaxial thruster.

A. The 2D Thruster and the Equivalent Coaxial Thruster Geometry

A 2D MPDT with its dimensions similar to the experimental straight-anode thruster[4] is chosen as the base geometry for this study. This thruster will be referred here as the 2D thruster. Although the thruster consists of a straight anode, a diverging insulator section is fixed at the exit. As mentioned before, this is done primarily to avoid an abrupt expansion region that would cause numerical instability to the inviscid flow model and this diverging section also converts any available pressure thrust into momentum component.

The theoretical electromagnetic thrust as a function of current and geometry for a coaxial thruster[19] and for a 2D thruster[4] are

$$F_{em,coax} = \frac{\mu_0 I^2}{4\pi}\ln\left(\frac{d_{a,coax}}{d_{c,coax}} + \frac{3}{4}\right) \tag{24}$$

$$F_{em,2D} = \frac{\mu_0 I^2}{4W}\left(\frac{(d_{a,2D} - d_{c,2D})}{2} + \alpha\frac{d_c}{2}\right) \tag{25}$$

Neglecting the second term in the above expressions, which represent the cathode tip effect they are equated to obtain the anode diameter for the coaxial thruster.

$$d_{a,coax} = \exp\left(\frac{(d_{a,2D} - d_{c,2D})\pi}{2W}\right) \times d_{c,coax} \tag{26}$$

The coaxial thruster termed, Coaxial-I is modeled for equal electromagnetic thrust compared to the 2D thruster using the above expression. Another coaxial thruster (referred here as Coaxial-II) with anode diameter twice of that of Coaxial-I was considered to double the electromagnetic thrust obtained in Coaxial-I thruster.

The dimensions of the 2D thruster are:

$$d_{a,2D} = 28mm,\ d_{c,2D} = 8mm \text{ and } W = 84mm$$

Assuming the cathode dimensions (length and diameter) for coaxial thrusters to be same as that of the 2D thruster, Eq. (26) was used to obtain the anode diameter of Coaxial-I and this diameter value is doubled for the corresponding Coaxial-II anode diameter. Figure. 1 shows a schematic diagram of the MPD thruster common to both 2D and coaxial geometries. The dimensions of the 2D, Coaxial-I and Coaxial-II thrusters are given in Table. 1

Table 1. Dimensions of thrusters used for the study

Notation	Description	2D	Coaxial-I	Coaxial-II
L1	Anode length	50.0	50.0	50.0
L2	Cathode length	10.0-50.0	10.0-50.0	10.0-50.0
L3	Total thruster length	120.0	120.0	120.0
D1	Diameter/Height at the thruster inlet	28.0	11.682	19.628
D2	Diameter/Thickness of the cathode	8.0	8.0	8.0
D3	Diameter/Height at the thruster exit	80.0	19.654	33.176

Dimensions are in mm

B. The Simulation Matrix

The computations were carried out at various inlet mass flow rates (0.625 g/s, 2.5 g/s and 10 g/s) and currents (2, 6, 10, 14 and 18 kA) for the cathode lengths varying from 10 mm-50 mm. Three cathode lengths (10 mm, 30 mm and 50 mm) were chosen for the three thrusters, except for some cases where a finer variation in cathode length (in steps of 5 mm) was maintained to get a better insight into the trend. A mesh size of 151×31 with uniformly spaced grids were used in most of the cases. Clustering of grids near the inlet was done for cases where an improvement in the numerical

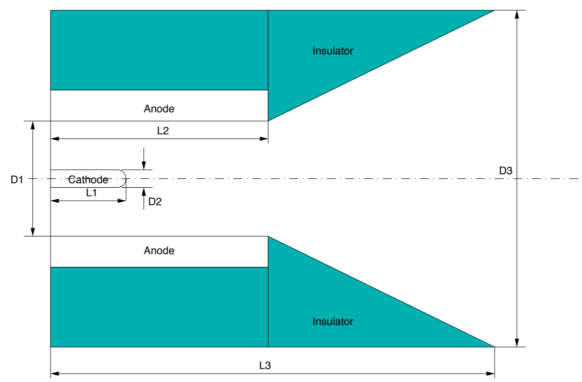

Figure 6. Schematic view of thruster common to 2D and coaxial geometries

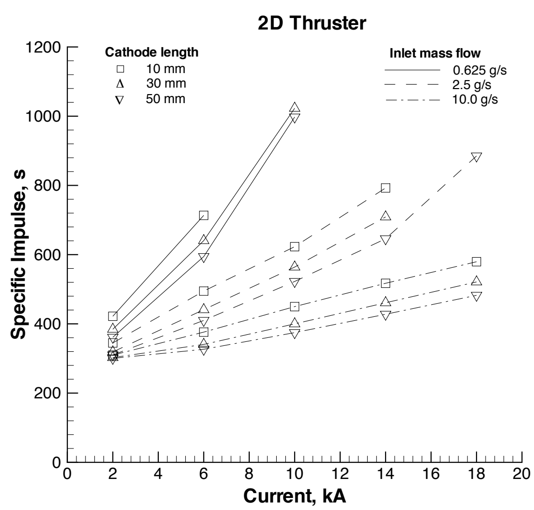

Figure 7. Variation of I_{sp} with current for 2D thruster

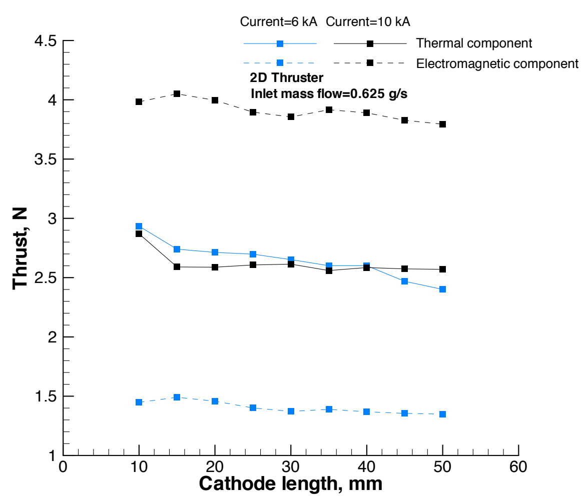

Figure 8. Thermal and Electromagnetic components of thrust as a function of cathode length for 2D thruster

convergence was required. Numerical instability was observed at low mass flow rates and high currents, whether the cause of these is physical or numerical is yet to be ascertained. The results for these cases have not been included here. The inclusion of Hall-effect did not have effect on the thruster performance but resulted in numerical difficulties at high currents therefore, has been switched off in the present study.

C. Effect of Cathode length in 2D thruster

Figure. 7 shows the plot of I_{sp} as a function of current for various mass flow rates and different cathode lengths. I_{sp} increases with the increase in current. This rate of increase in I_{sp} with current is higher at lower mass flow rates. The variation in I_{sp} for the three different cathode lengths (10 mm, 30 mm and 50 mm) can be seen at from these curves, which indicate higher values of I_{sp} for short cathodes. This trend of increase in I_{sp} with cathode length is observed at all mass flow rates. It can also be observed that the change in I_{sp} with cathode length is lower at both low and high currents compared to the intermediate values. Since the total thrust produced is lower at low currents, all thruster lengths exhibit low I_{sp} in this region of current. As the current is increased, the I_{sp} variation between each cathode length increases through the intermediate values of current and then decreases again at higher currents. This trend is clearly notable for the mass flow rate of 0.625 g/s. From the available data points for other mass flow rates (2.5 g/s and 10 g/s), it is expected that the I_{sp} curves follow the same trend at much higher values of applied current.

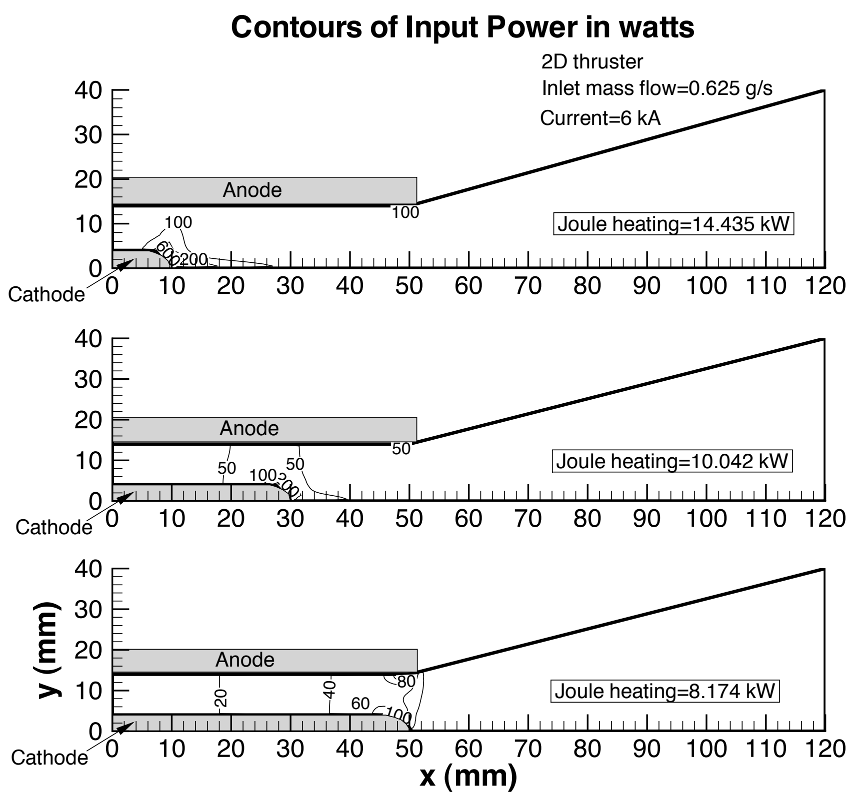

Figure 9. Input power distribution throughout the thruster at different cathode lengths (10 mm, 30 mm, and 50 mm) for 2D thruster

To examine the effect of cathode length variation closely, the cathode length was varied from 10 mm to 50 mm in steps of 5 mm for the specific case of 0.625 g/s mass flow rate and two different currents (6 kA and 10 kA). Figure. 8 shows a plot of the components of thrust as a function of cathode length. One can note that the thermal thrust is higher than the electromagnetic thrust at 6 kA current whereas the electromagnetic component is higher than the thermal component at 10 kA current. As the cathode length is varied from 10 mm to 50 mm the drop in thermal thrust is larger compared to drop in electromagnetic thrust. For the 6 kA case, the thermal thrust drops continuously as cathode length is increased from 5 mm to 10 mm but in case of 10 kA the drop is confined to only shorter lengths (about 15 mm). The thruster performance (thrust and specific impulse) is also confined to the region of cathode length less than 15 mm, indicating that sensitivity to change in cathode length to be higher at shorter lengths. This implies that cathode length variation is mostly a thermal phenomenon. This is further corroborated by weaker dependence on thrust and specific impulse when thruster operation is shifted from thermal to electromagnetic regime. Here we define "electromagnetic regime" as regions where total thrust is dominated by electromagnetic component ($F_{total}/F_{em} < 2$). To examine further effect of cathode length on Ohmic heating we look at figure. 9 which shows the contour plot of input power at 10 mm, 30 mm and 50 mm cathode lengths for a mass flow rate of 0.625 g/s and 6 kA current. One can note that there is an increase in the input power as the cathode length decreases. This is mainly caused by Joule heating/Ohmic dissipation (j^2/σ) as the shortening of cathode decreases the sectional area of the current passage thereby increasing the current density through it. This heating is responsible for the increase in the thermal component of thrust.

D. Effect of Cathode Length in coaxial thrusters

1. The Coaxial-I Thruster:

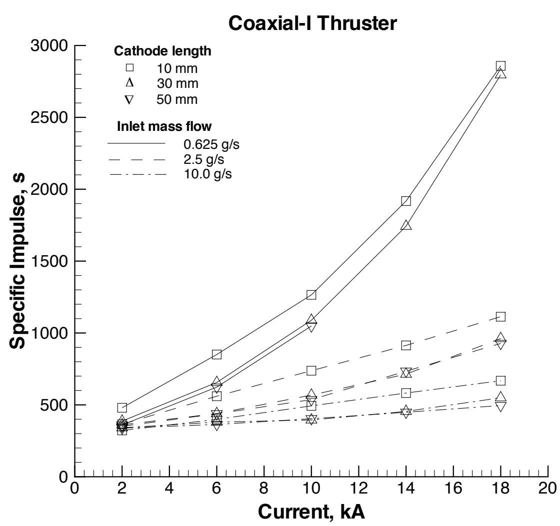

Figure 10. Variation of I_{sp} with current for Coaxial-I thruster

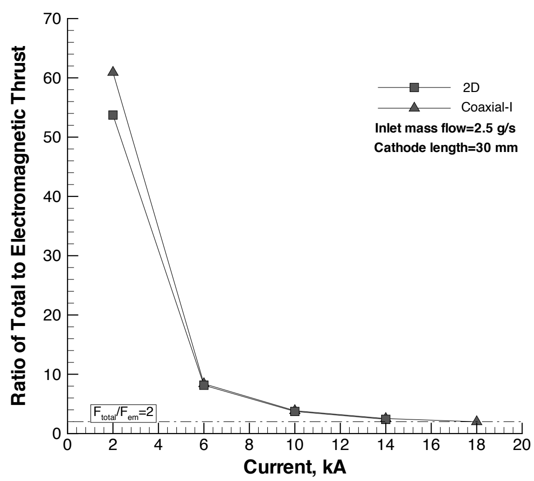

Figure 11. Ratio of total to electromagnetic thrust as a function of current for 2D and Coaxial-I thrusters

The Coaxial-I thruster, which is electromagnetic thrust equivalent of the 2D thruster exhibits qualitatively similar performance characteristics. This can be seen from the plot of I_{sp} with current for various mass flow rates and cathode lengths in Fig. 10. The I_{sp} variation with current and cathode length shows a trend similar to the 2D thruster. However the shorter cathode (here 10 mm cathode) performs much superior to the 2D counterpart. It can also be seen that the range of current for which numerical solution could be obtained for a given mass flow rate is higher in Coaxial-I thruster compared to the 2D thruster. This resulted in higher values of I_{sp}. Figure. 11 shows the plot of ratio of total to electromagnetic thrust as a function of current for the 2D thruster and the Coaxial-I thruster. A line drawn across at a value of $F_{total}/F_{em}=2$ indicates the demarcation of thermal and electromagnetic regimes. It can be seen that the both 2D and Coaxial-I thrusters enter into electromagnetic regime of operation in a similar manner. Figure. 12 shows the variation of I_{sp} with cathode length at 0.625 g/s mass flow rate and 10 kA current. The plot indicates that the I_{sp} variation is higher at shorter cathode lengths, as observed in the 2D thruster, but the slope of I_{sp}

with cathode length is steeper in the Coaxial-I thruster compared to the 2D counterpart indicating the higher sensitivity of the coaxial thruster to variation in cathode length at shorter cathode lengths. Since the input power reduces with the increase in cathode length, which was observed from Fig. 9 for the 2D thruster, the similar reduction in input power for the coaxial thruster causes an increase in thrust to power ratio (TPR) as seen in Fig. 13.

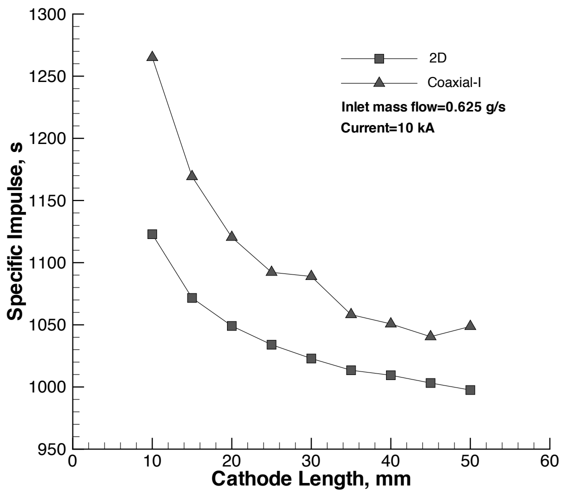

Figure 12. I_{sp} as a function of cathode length for 2D and Coaxial-I thrusters

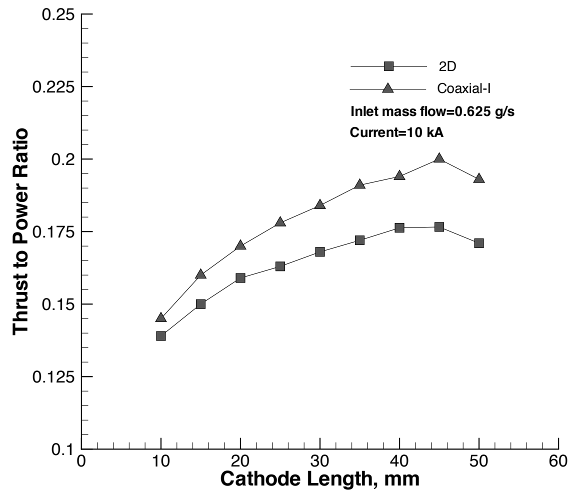

Figure 13. TPR as a function of cathode length for 2D and Coaxial-I thrusters

2. The Coaxial-II Thruster:

Coaxial-II thruster was designed to produce double the electromagnetic thrust compared to Coaxial-I (double anode diameter of Coaxial-I for same cathode diameter).[19] Figure. 14 presents variation in I_{sp} with input current at mass flow rates of 0.625 g/s, 2.5 g/s and 10 g/s for the three cathode lengths (10 mm, 30 mm and 50 mm). Though the overall trend is similar to Coaxial-I, the magnitude of I_{sp} is higher for Coaxial-II at a given input current and mass flow rate. Further the change in cathode length is seen to have lesser effect on I_{sp} compared to Coaxial-I. For example at mass flow rate of 0.625 g/s and input current of 6 kA the I_{sp} increased from 620-850 s (lower for 50 mm long cathode and higher for 10 mm long cathode) for Coaxial-I to 960-1100 s for Coaxial-II. At this point Coaxial-I is in thermal regime where as Coaxial-II is in the electromagnetic dominant thrust regime. This corroborates the role of Ohmic dissipation in causing cathode length dependency in thruster. Figure. 15 shows the thermal and electromagnetic thrust components with input current for the three thrusters at 2.5 g/s and 30 mm cathode length. The Coaxial-II thruster shows an increase in the electromagnetic thrust compared to Coaxial-I. Interestingly the thermal component of thrust is seen to be similar for all the three thrusters. It should be noted that only electromagnetic thrust component was matched

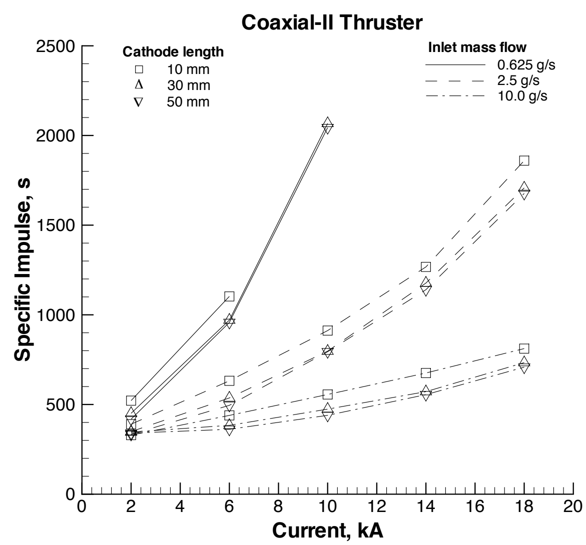

Figure 14. Variation of I_{sp} with current for Coaxial-II thruster

between 2D and Coaxial-I in deciding the thruster geometry. Figure 16. presents thrust components of Coaxial-I and Coaxial-II with cathode length at two different input currents (6 kA and 14 kA) and at a mass flow rate of 2.5 g/s. At 6 kA current both thruster have stronger thermal thrust component but at 14 kA electromagnetic thrust dominates the total thrust. The figure also illustrates the larger variation in thrust with cathode length is coming from the thermal component. Thus the sensitivity in the variation of thrust or specific impulse with cathode length is lesser for Coaxial-II when the two thrusters are operated at a same current, which is because the Coaxial-II thruster enters into electromagnetic regime at lower currents compared to Coaxial-I thruster and because of its higher electromagnetic thrust component.

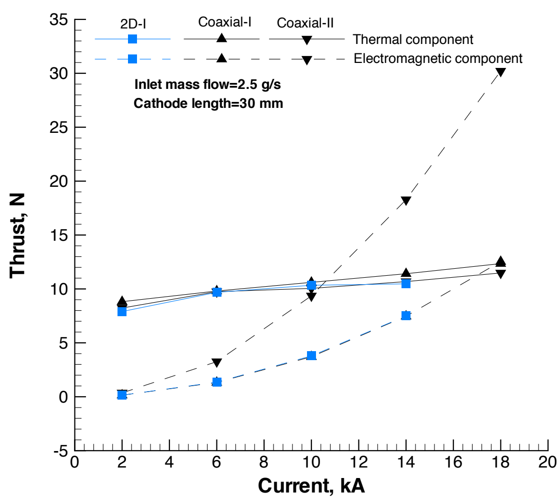

Figure 15. Thermal and electromagnetic components of thrust for 2D, Coaxial-I and Coaxial-II thrusters as a function of current

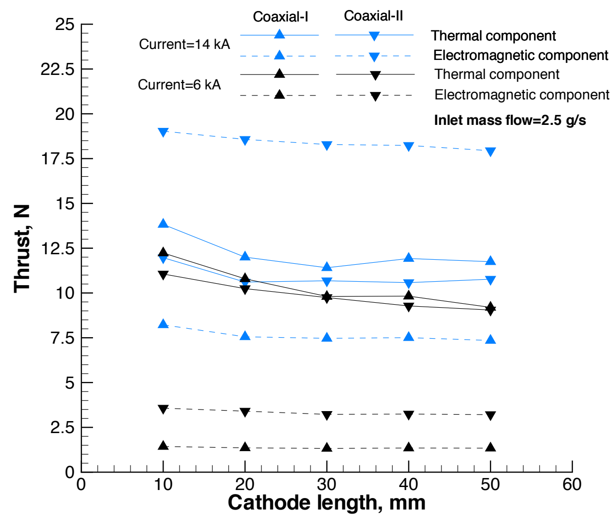

Figure 16. Thermal and electromagnetic components of thrust for Coaxial-I and Coaxial-II as a function of cathode length at 6 kA and 14 kA currents

IV. Conclusion

Effect of cathode length on performance of a 2D MPDT and an equivalent coaxial thruster was carried out numerically. Computations were performed over a matrix of mass flow rates and current for various cathode lengths. Based of these computations the following conclusions may be drawn:

1) At small currents (<2 kA) where total thrust is small and at high currents where the total thrust is dominated by electromagnetic component, the cathode length had little effect on thruster performance. Under both these conditions thermal component of thrust has small contribution. However at intermediate currents, in Ohmic heating dominated regions, the shorter cathode gave increasingly better performance. This shows that cathode length effect on thruster performance is primarily due to Ohmic heating.

2) It is also noted that the rate of drop in thrust and specific impulse with cathode length decreases with increase in cathode length. That is the thruster performance is more sensitive to changes in length in short cathode. In comparison to the 2D MPDT the coaxial thrusters are expected to show higher sensitivity at short cathode lengths.

3) It is interesting to note that the thermal component of thrust did not get altered between 2D and Coaxial-I thrusters even though only the electromagnetic component was matched between them. This effect was also observed between Coaxial-I and Coaxial-II where only the electromagnetic component of thrust increased.

References

[1]Kuriki, K., Kunii, Y., and Shimizu,Y., “Idealized Model for Plasma Acceleration in an MHD channel”, *AIAA Journal*, 21(3), 322–326, 1983.

[2]Martinez-Sanchez, M., “Structure of Self-field Accelerated Plasma Flows”, *Journal of Propulsion and Power*, 1(7), 56–64, 1994.

[3]Nakayama, T., Toki, K., and Kuriki, K., “Quantitative Imaging of the Magnetoplasmadynamic Flow Field”, *Journal of Propulsion and Power*, 8(6), 1217–1223, 1992.

[4]Funaki, I., Toki K., Kuriki K., “Electrode Configuration Effect on the Performance of a Two-Dimensional Magnetoplasmadynamic Arcjet”, *Journal of Propulsion and Power*, 14(6) 1043-1048, 1998.

[5]Funaki, I., Toki K., Kuriki K., “Numerical Analysis of a Two-Dimensional Magnetoplasmadynamic Arcjet”, *Journal of Propulsion and Power*, 13(6) 789-795, 1997.

[6]Kubota, K., Funaki, I., and Okunu, Y., “Numerical study of Electrode Geometry Effects on Flow Field in Two-dimensional MPD Thrusters”, *In 30 th International Electric Propulsion Conference*, Paper No. IEPC-2007-87, 2007.

[7]Shoji, I. and I. Kimura, “Effect of Thruster Length on MPD Flows”, *In Proceedings of Faculty of Tokai University*, Vol. 19, 1994.

[8]Lapointe, M. R., “Numerical Simulation Self-field MPD Thrusters”, NASA-CR-187168, 1991.

[9]G. W. Sutton and A. Sherman, *Engineering Magnetohydrodynamics*, Dover Publications, Inc., New York, 1965.

[10]Auweter-Kurtz, M., Kurtz, H. L., Schrade, H. O., and Sleziona, P. C., “Numerical Modeling of Flow Discharge in MPD Thrusters,” *Journal Propulsion and Power*, 5, pp. 49-55, 1989.

[11]Blazek, J., *Computational Fluid Dynamics: Principles and Applications*, Elsevier, 2005.

[12]Fletcher, C. A. J. , *Computational Techniques for Fluid Dynamics- Vol. 1 and 2*, Springer-Verlag, 1988.

[13]Wendt, J. F.(Editor), *Computational Fluid Dynamics-An Introduction*, Springer-Verlag, 2009.

[14]Hall, M., “A Vertex-Centroid Scheme for Improved Finite-Volume Solution of the Navier-Stokes Equations”, *AIAA-91-1540*, 1991.

[15]Hirsch, C., *Numerical Computation of Internal and External Flows-Vol. 1*, Wiley,1988.

[16]Chanty, J.M.G. and Martinez-Sanchez M., “Two-Dimensional Numerical Simulation of MPD Flows”, *19th IEPC*, AIAA-87- 1090, May 1987.

[17]Crumpton, P. I., Mackenzie, J. A., and Morton, K. W., “Cell Vertex Algorithms for the Compressible Navier-Stokes Equations”, *Journal Computational Physics*, 109, pp. 1-15, 1993.

[18]Niewood, E. H., “Transient One Dimensional Numerical Simulation of Magnetoplasmadynamic Thrusters”, Master’s thesis, MIT, Boston, Massachusetts, USA, 1989.

[19]Jahn, R. G., *Physics of Electric Propulsion*, McGraw-Hill, New York, 1968.